Document Version
Final published version

Citation (APA)
Wang, C. A., John, V., Tidjani, H., Yu, C. X., Ivlev, A. S., Déprez, C., van Riggelen-Doelman, F., Woods, B. D., Hendrickx, N. W., Lawrie, W. I. L., Stehouwer, L. E. A., Oosterhout, S. D., Sammak, A., Friesen, M., Scappucci, G., de Snoo, S. L., Rimbach-Russ, M., Borsoi, F., & Veldhorst, M. (2024). Operating semiconductor quantum processors with hopping spins. *Science (New York, N.Y.), 385*(6707), 447-452. https://doi.org/10.1126/science.ado5915

QUANTUM COMPUTING

Operating semiconductor quantum processors with hopping spins

Chien-An Wang[1], Valentin John[1], Hanifa Tidjani[1], Cécile X. Yu[1], Alexander S. Ivlev[1], Corentin Déprez[1], Floor van Riggelen-Doelman[1], Benjamin D. Woods[2], Nico W. Hendrickx[1], William I. L. Lawrie[1], Lucas E. A. Stehouwer[1], Stefan D. Oosterhout[3], Amir Sammak[3], Mark Friesen[2], Giordano Scappucci[1], Sander L. de Snoo[1], Maximilian Rimbach-Russ[1], Francesco Borsoi[1]†, Menno Veldhorst[1]*†

Qubits that can be efficiently controlled are essential for the development of scalable quantum hardware. Although resonant control is used to execute high-fidelity quantum gates, the scalability is challenged by the integration of high-frequency oscillating signals, qubit cross-talk, and heating. Here, we show that by engineering the hopping of spins between quantum dots with a site-dependent spin quantization axis, quantum control can be established with discrete signals. We demonstrate hopping-based quantum logic and obtain single-qubit gate fidelities of 99.97%, coherent shuttling fidelities of 99.992% per hop, and a two-qubit gate fidelity of 99.3%, corresponding to error rates that have been predicted to allow for quantum error correction. We also show that hopping spins constitute a tuning method by statistically mapping the coherence of a 10–quantum dot system. Our results show that dense quantum dot arrays with sparse occupation could be developed for efficient and high-connectivity qubit registers.

Loss and DiVincenzo proposed hopping of electrons between two quantum dots as an efficient method for coherent spin control (*1*). By applying discrete pulses to the quantum dot gates, a single spin can be transferred between qubit sites with differently oriented spin quantization axes, thereby enabling two-axis control of the qubit. Universal quantum logic is then achieved through a tunable exchange interaction between spins residing in different quantum dots. That work initiated the field of semiconductor spin qubits and inspired more than two decades of extensive research, but a successful implementation of Loss and DiVincenzo's initial proposal has remained elusive because of experimental challenges (*2*).

Alternative methods for coherent single-spin control have emerged, including electron spin resonance (*3*, *4*) and electric dipole spin resonance using either micromagnets (*5*, *6*) or spin-orbit interaction (*7*–*10*) to enable a coupling between the electric field and the spin degree of freedom. However, all of these methods rely on resonant Rabi driving and require high-power, high-frequency analog control signals that already limit qubit performance in small quantum processors (*11*–*13*). The development of local, efficient, low-power control mechanisms of semiconductor spins is now a key driver (*14*–*16*). To this end, qubits encoded in multiple spins and in multiple quantum dots, such as singlet-triplet, hybrid, and exchange-only qubits, have been investigated as possible platforms (*2*). Although these qubit encodings have enabled digital single-qubit control, they also come with new challenges in coherence, control, and creation of quantum links. For example, the exchange-only qubits are susceptible to leakage outside of their computational subspace and require four exchange pulses to execute an arbitrary single-qubit gate and >12 exchange pulses for a single two-qubit gate (*17*–*19*).

Here, we demonstrate that single-spin qubits can be operated using baseband control signals, as envisaged in the original proposal for quantum computation with quantum dots (*1*). We used hole spins in germanium quantum dots, in which the strong spin-orbit interaction gives rise to an anisotropic g-tensor that is strongly dependent on the electrostatic and strain environment (*20*). We harnessed the resulting differences in the spin quantization axis between quantum dots (*21*, *22*) to achieve high-fidelity single-qubit control using discrete pulses by shuttling the spin between quantum dot sites. A key advantage in such a hopping-based operation is that the spin rotation frequency is given by the Larmor precession. The latter remains sizeable even at small magnetic fields where quantum coherence is substantially improved (*23*, *24*). This enabled us to perform universal quantum control with error rates exceeding the thresholds predicted for practical quantum error correction (*25*) while also operating with low-frequency baseband signals. We then exploited the differences in quantization axes to map the spin dephasing times and g-factor distributions of an extended 10–quantum dot array, thereby efficiently gathering statistics on relevant metrics in large spin qubit systems.

High-fidelity single-qubit operations and long qubit coherence times at low magnetic field

A large difference in the orientation of the spin quantization axes between quantum dots is essential for hopping-based qubit operations. Holes in planar germanium heterostructures manifest a pronounced anisotropic g-tensor, with an out-of-plane g-factor, $g_\perp$, that can be two orders of magnitude larger than the in-plane component, $g_{||}$ (*20*, *24*, *26*, *27*). Consequently, a small tilt of the applied magnetic field from the in-plane g-tensor will lead to a strong reorientation of the spin quantization axis in the out-of-plane direction. Subsequently, when an in-plane magnetic field is applied, the orientation of the spin quantization axis is highly sensitive to the local g-tensor, and thus to confinement, strain, and electric fields, thus becoming a site-dependent property (*21*, *24*, *28*, *29*). Here, we exploited this aspect to establish hopping-based quantum operations in two different devices: a four-quantum dot array (*30*) arranged in a 2 × 2 configuration and a 10–quantum dot system arranged in a 3-4-3 configuration.

We populated the four-quantum dot array with quantum dots Dm with $m \in [(1, 4)]$ with two hole spins, Q_A and Q_B, which can be shuttled between quantum dots by electrical pulses on the gate electrodes (Fig. 1A). A magnetic field up to 40 mT was applied to split the spin states and positioned in-plane up to sample-alignment accuracy [see the materials and methods (*31*)]. The relatively small magnetic fields ensured that the maximum qubit frequency (140 MHz) and its corresponding precession period (7 ns) were within the bandwidth of the arbitrary waveform generators used. In combination with engineered voltage pulses with subnanosecond resolution (*21*) [(*31*), section 1], we were able to shuttle a spin qubit to an empty quantum dot and thereby accurately change the qubit precession direction several times within one precession period. Altogether, this enables efficient single-qubit control through discrete voltage pulses (Fig. 1B).

The net effect of a multiple-shuttle protocol is a rotation $R(\hat{n},\theta)$ of the spin state around an axis $\hat{n}$ and with an angle θ. To implement a specific rotation such as the quantum gate $X_{\pi/2}$, the number of required shuttling steps depends on the angle between the two quantization axes. Because of the large angle between the axes of D1 and D4, $\theta_{14} > 90°/4 = 22.5°$, a pulse consisting of four shuttling steps is sufficient to realize a precise quantum gate $X_{\pi/2,\mathrm{A}}$ [(*31*), sections 2 and 3]. As outlined on the top right panel of Fig. 1C, such a four-shuttle pulse moves the spin between D1 and D4 four times with waiting periods t_1 and t_4, respectively. By measuring the spin-flip probability of Q_A, $P_{A\uparrow}$, after two consecutive rotations $R(\hat{n},\theta)^2$, we could determine the values of t_1

---

[1]QuTech and Kavli Institute of Nanoscience, Delft University of Technology, 2600 GA Delft, Netherlands. [2]Department of Physics, University of Wisconsin-Madison, Madison, WI 53706, USA. [3]QuTech and Netherlands Organisation for Applied Scientific Research (TNO), 2628 CK Delft, Netherlands.
***Corresponding author. Email: m.veldhorst@tudelft.nl**
†These authors jointly supervised this work.

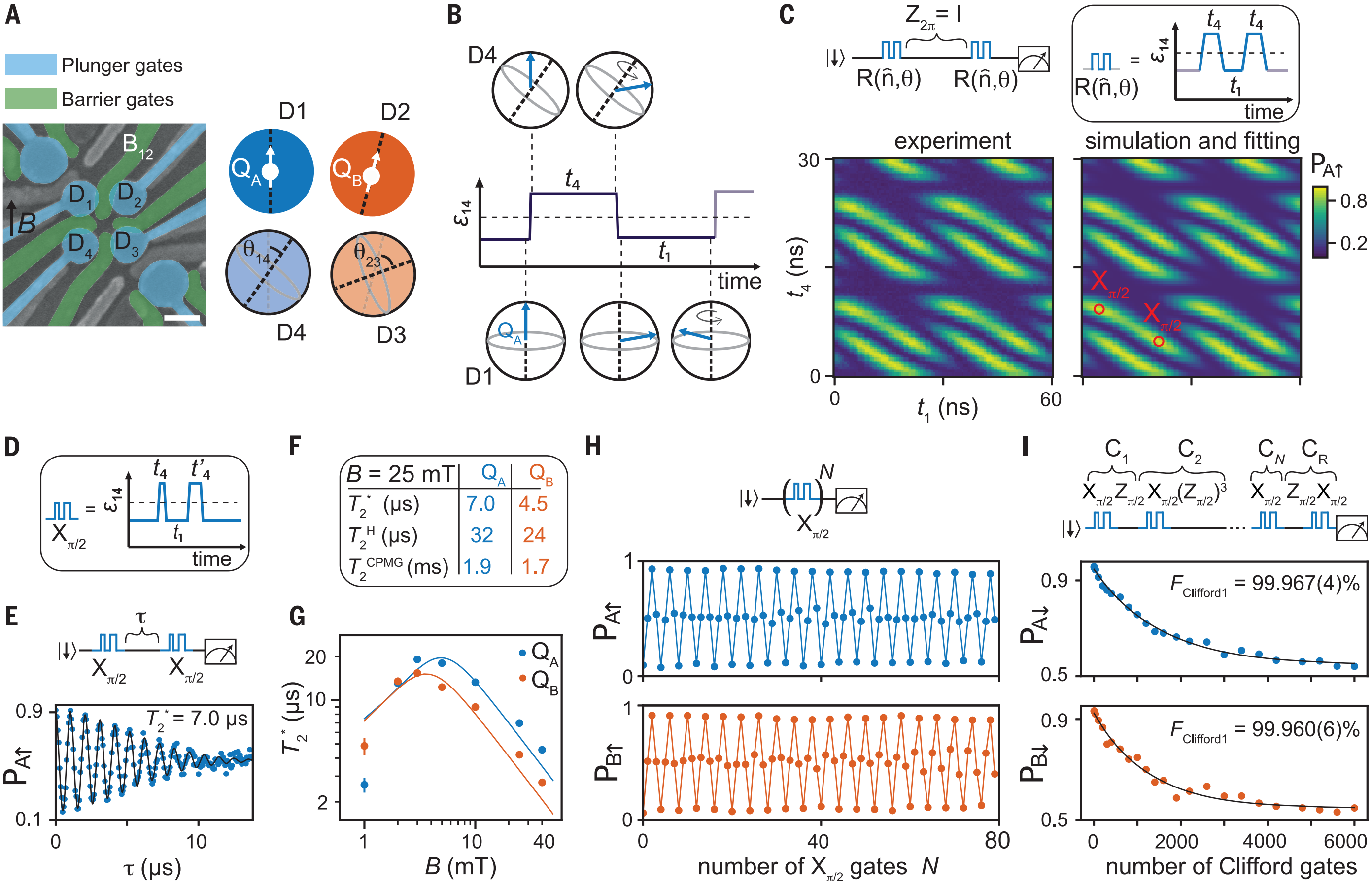

B = 25 mT	Q_A	Q_B
T_2^* (μs)	7.0	4.5
T_2^H (μs)	32	24
T_2^{CPMG} (ms)	1.9	1.7

Fig. 1. High-fidelity hopping-based single-qubit operations and long qubit coherence times at low magnetic field. (**A**) Left: scanning electron microscopy image of the 2 × 2 quantum dot array device (*30*), including gate-defined charge sensors at two corners. Scale bar, 100 nm. Right: schematic of the two spin qubits, Q_A and Q_B. The black dashed lines mark the relative quantization axis direction in the quantum dot pair D1-D4 (D2-D3), with the angle θ_{14} (θ_{23}). (**B**) Example of a baseband pulse $\varepsilon_{14}(t)$ used to manipulate qubit Q_A by shuttling the spin back and forth between quantum dots D1 and D4 and allowing the spin to precess in the individual quantum dots for the time t_4 and t_1. (**C**) Tune-up procedure of a four-shuttle pulse for the $X_{\pi/2}$ gate of Q_A at 20 mT. Top: pulse sequence of the experiment. Bottom left: measured spin-up probability $P_{A\uparrow}(t_1,t_4)$. Bottom right: simulation results. The red markers identify the timings for implementing an $X_{\pi/2,A}$ gate and correspond to the maximal spin-up probability. The markers are periodic in t_1 and t_4, but for clarity we only plot a few of them. (**D**) Calibrated pulse for $X_{\pi/2,A}$ gate with unequal wait time t_4 and t_4'. (**E**) Free induction decay obtained from Ramsey experiments at 25 mT. (**F**) Coherence times T_2^*, T_2^H, and $T_2^{CPMG\text{-}512}$ of both qubits at 25 mT. (**G**) T_2^* as a function of magnetic field. The data points are fitted with an effective model including electric noise and nuclear noise [(*31*), section 5]. (**H**) Spin-up probability after applying a varying number of $X_{\pi/2}$ gates on each qubit. (**I**) Example of a pulse sequence in Q_A single-qubit randomized benchmarking and the measurement results of both qubits. The uncertainties are obtained from bootstrapping with 95% confidence intervals.

and t_4 where $P_{A\uparrow}$ is maximal, which occurs when $R(\hat{n},\theta) = X_{\pi/2,A}$.

Although this method allows calibration of the pulse timing to compose an $X_{\pi/2,A}$ gate, it is not necessarily the optimal trajectory. Different choices of (t_1,t_4) are possible (Fig. 1C), including a composition of four-shuttle pulses with different waiting times in D4. The latter implementation allows for the construction of gates with a rotation angle θ less sensitive to Larmor frequency fluctuations in D4. We constructed such a gate by fitting the data in Fig. 1C to an effective model and determined the quantization axes angle θ_{14} between the quantum dots D1 and D4, the individual Larmor frequencies, and the effective precession time during the ramp. Through simulation of the qubit dynamics, we designed a more noise-resilient $X_{\pi/2,A}$ gate based on four shuttling steps with unequal wait times t_4 and t_4' in D4 (Fig. 1D). Following the same approach, we designed an $X_{\pi/2,B}$ gate for Q_B that only requires a two-shuttle protocol because the angle of the difference in quantization axes of D2 and D3, θ_{23}, is very close to 45° [(*31*), section 3].

We further calibrated the pulse timing using repetition sequences, as shown in Fig. 1H, and in AllXY sequences (*32*) [(*31*), section 3]. The $Y_{\pi/2}$ gate in the AllXY sequences was realized by $Y_{\pi/2} = Z_{\pi/2}X_{\pi/2}Z_{3\pi/2}$, and the $Z_{\pi/2}$ gate was implemented by idling the qubit for the time defined by its precession in the lab frame. The calibrated $X_{\pi/2}$ gates had a total gate time of 98 (35) ns for Q_A(Q_B), corresponding to effective qubit rotation frequencies of 2.6 (7.1) MHz, considerable compared with the Larmor frequencies $f_{A(B)}$ = 42.6 (89.5) MHz at the in-plane magnetic field of 25 mT.

The high ratio between qubit rotation and Larmor frequency results in low power dissipation, which is a critical aspect for scaling up quantum processors (*33*). To compare the power consumption of the hopping-based single-qubit control with the electric dipole spin resonance technique, we defined the required number of voltage oscillations to flip a qubit, N_{cycles}, and the derived energy efficiency, $\eta = 1/N_{\text{cycles}}$, which we found largely determines the power dissipation under the assumption that dielectric losses are dominant over other dissipation mechanisms [(*31*), section 4]. For our system, we estimate an efficiency of η = 25(50)% for Q_A(Q_B). By comparison, previous demonstrations of

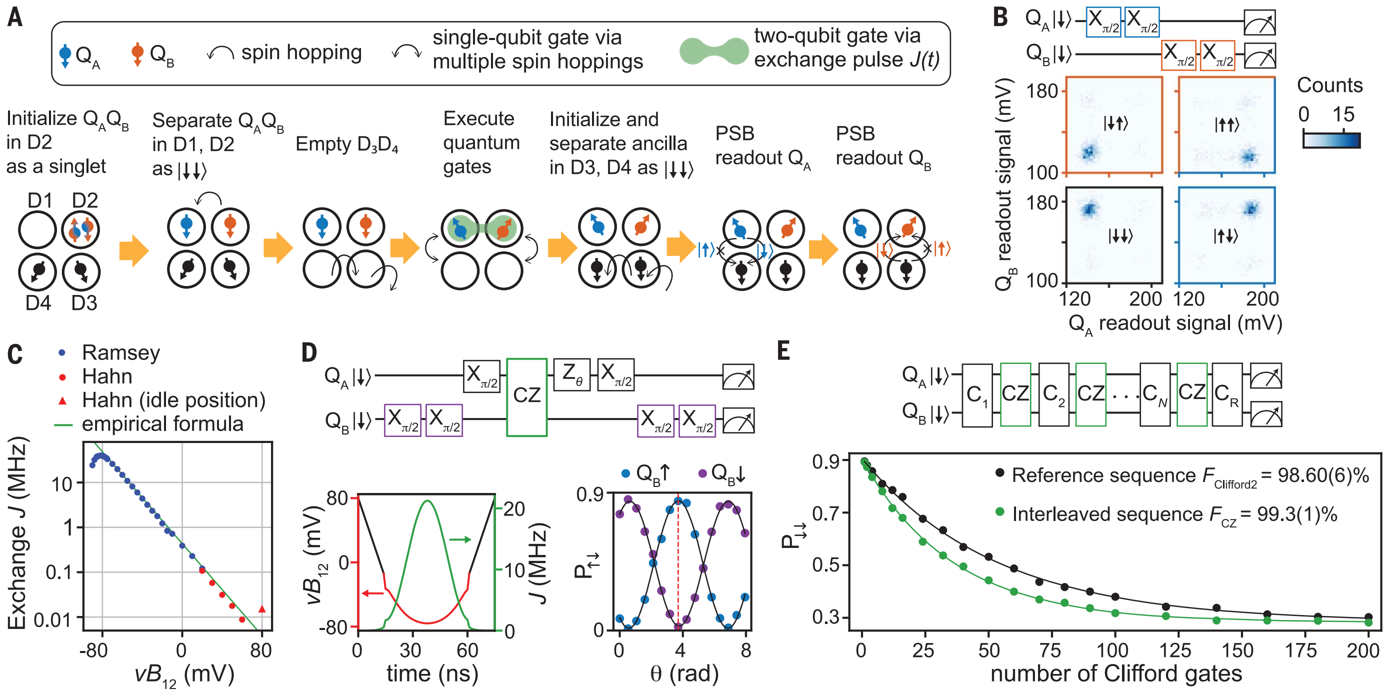

Fig. 2. High-fidelity two-qubit gate in germanium. (**A**) Schematics of two-qubit initialization, manipulation, and individual readout. Q_AQ_B was initialized by relaxing to the singlet ground state in D2 and then adiabatically moving one spin to D1. Quantum circuits consisting of single-qubit gates (spin hoppings) and two-qubit gates [exchange pulse $J(t)$] were performed. The final quantum state was read out by preparing ancillary spins and then performing two PSB readouts. In each readout, the chemical potentials of the quantum dots were pulsed such that the spin can either move to the neighboring dot (indicated by arrows) or stay in the original dot (indicated by arrows with × markers), with probabilities depending on the spin state $Q_{A(B)}$. (**B**) Two-dimensional histograms of the sensor signals formed by 500 single-shot measurements for four different two-qubit states prepared by applying $X_{\pi/2,A(B)}$ gates. (**C**) Exchange coupling as a function of virtual barrier gate vB_{12}, measured by Ramsey (Hahn echo) experiments in the large (small) coupling regime. The idle position corresponds to the barrier voltage where single qubit gates were performed, but at slightly different plunger gate voltage. The empirical formula for mapping vB_{12} and J is detailed in (*31*), section 12. The bending on the left side of the plot results from the energy level anticrossing when $J \sim f_A$. (**D**) The voltage pulse of the CZ gate was shaped to have exchange $J(t)$ in the form of a Hamming window, as illustrated on the bottom left. The CZ gate calibration circuit for single-qubit phases is on the top, with the measurement outcome plotted on the bottom right. The target qubit (Q_A) phase depends on the control qubit Q_B being in the state ↓ in blue (↑ in purple). The red dashed line marks the required single-qubit phase of Q_A for the CZ gate. (**E**) Gate sequence and measurement result of two-qubit interleaved RB.

high-fidelity universal qubit logic in silicon exhibited η in the range of 0.04 to 0.07% (*11, 12, 15*). Moreover, despite applying sizeable amplitudes to move the spins between localized orbitals of adjacent quantum dots, we still obtained a factor of 20 reduction in power dissipation with respect to the electric dipole spin resonance technique [(*31*), section 4]. Engineering lower required pulse amplitudes and increasing the orthogonality of the spin quantization axes will enable a further reduction of the dissipated power. Furthermore, the hopping-based approach can simplify the signal delivery and required control electronics and thus alleviate the detrimental heating effects.

Having established universal single-qubit control, we used the set of gates $\{X_{\pi/2}, Y_{\pi/2}\}$ to investigate the qubit coherence times at low magnetic fields. By using a Ramsey sequence (Fig. 1E), we obtained a dephasing time T_2^* of 7.0 (4.5) μs at 25 mT for Q_A(Q_B), an order of magnitude larger than that measured at 1 T in the same sample (*23*, *30*). We were able to further extend the coherence times using Hahn and Carr-Purcell-Meiboom-Gill (CMPG) techniques, obtaining T_2^{H} = 32(24) μs and $T_2^{\mathrm{CPMG\text{-}512}}$ = 1.9(1.7) ms, respectively (Fig. 1F). The dependence of the dephasing times as a function of magnetic field (Fig. 1G) indicates that charge noise remains the main cause for decoherence for magnetic fields as low as 5 mT [(*31*), section 5].

We characterized the single-qubit gate fidelity using randomized benchmarking (RB) and gate set tomography (GST) (*34*–*36*) [(*31*), sections 6 and 7]. The results of RB with average Clifford fidelity (Fig. 1I) set the lower bounds of the $X_{\pi/2}$ average gate fidelity at $F_{X_{\pi/2},A} \geq$ 99.967(4)% and $F_{X_{\pi/2},B} \geq$ 99.960(6)%, consistent with the error modeling [(*31*), section 8]. Using GST, we benchmarked the $X_{\pi/2}$ and $Y_{\pi/2}$ gates, obtaining an average gate fidelity >99.9%. From the GST analysis, we infer that dephasing is the dominant contribution to the average gate infidelity. Taking into account the multiple shuttling steps to execute a single gate, we estimate a coherent shuttling fidelity per hop as high as F_{shuttle} = 99.992% [(*31*), section 9].

High-fidelity two-qubit exchange gate

We now focus on assessing the single-qubit and two-qubit gate performance in the two-qubit space. We implemented a two-qubit state preparation and measurement (SPAM) protocol (Fig. 2, A and B). For the state preparation, we adiabatically converted the two-spin singlet in D2 to the triplet Q_AQ_B = ↓↓. For the state measurement, we performed sequential Pauli spin blockade (PSB) readouts on Q_A and Q_B by loading ancillary spins from the reservoir and adiabatic conversion to the state ↓↓ in quantum dots D3 and D4. The difference in the effective *g*-factor between the quantum dots D1 and D2 allows for the construction of a controlled-Z (CZ) gate even at low magnetic fields. We did so by pulsing the virtual barrier gate voltage vB_{12}, which controls the exchange coupling J between Q_A and Q_B from 10 kHz to 40 MHz (Fig. 2C) [(*31*), sections 10 and 11]. Because the maximum exchange coupling

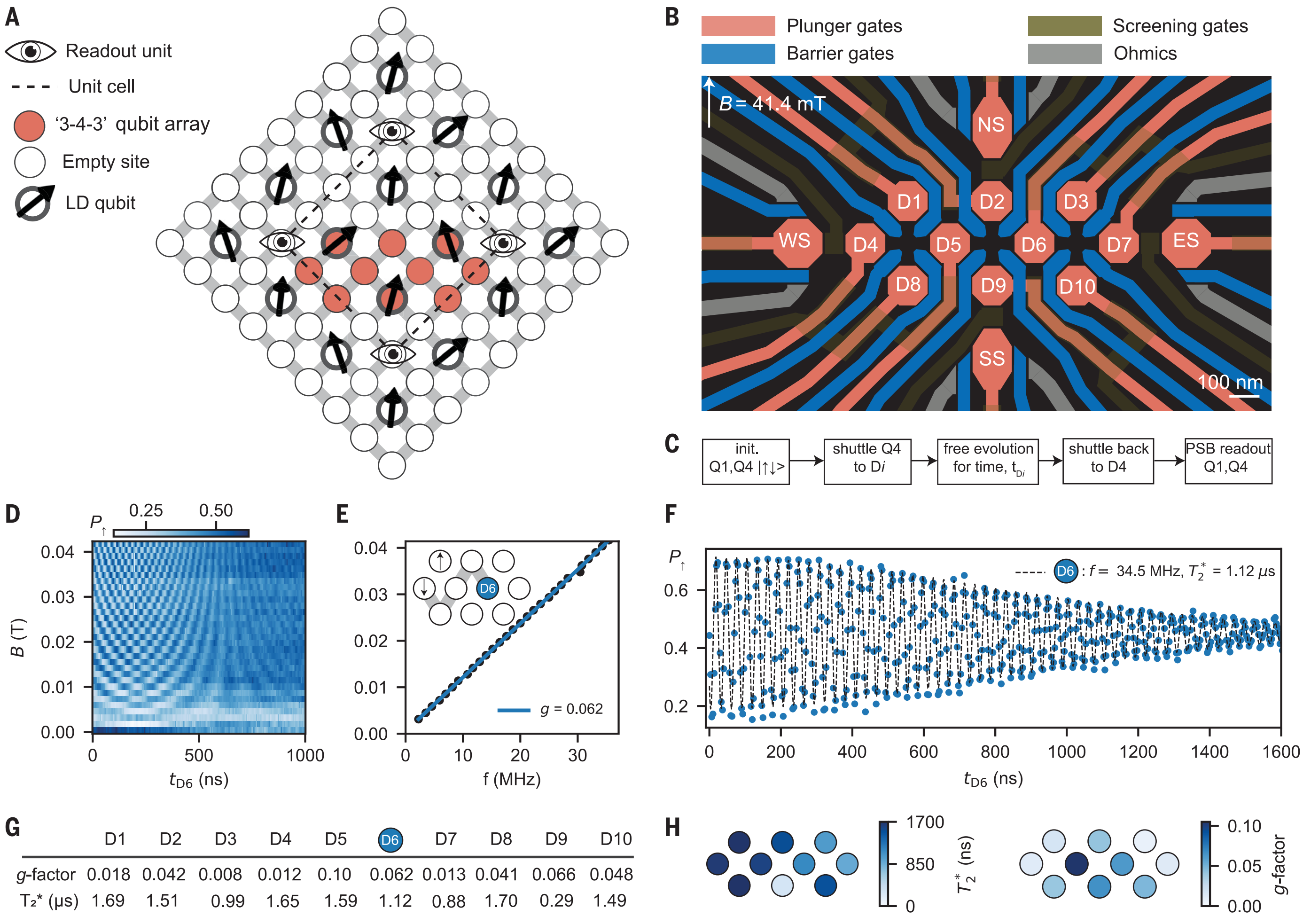

	D1	D2	D3	D4	D5	D6	D7	D8	D9	D10
g-factor	0.018	0.042	0.008	0.012	0.10	0.062	0.013	0.041	0.066	0.048
T_2* (μs)	1.69	1.51	0.99	1.65	1.59	1.12	0.88	1.70	0.29	1.49

Fig. 3. Hopping spins to benchmark large and high-connectivity quantum dot architectures. (**A**) Our vision of a semiconductor quantum computing architecture comprising hopping Loss-DiVincenzo (LD) spin qubits (black arrows), readout units (eyes), and empty quantum dot sites for shuttling operations. (**B**) Layout of the 10–quantum dot array, with gate-defined charge sensors labeled in analogy to the four cardinal points (NS, ES, WS, and SS). (**C**) Control sequence used to characterize the array. A spin originally in D4 was shuttled across the whole array, allowed to evolve at a certain quantum dot, and read out. (**D**) Qubit rotations induced by the difference in quantization axes as a function of idling time in quantum dot D6 and magnetic field. (**E**) D6 Larmor frequency, extracted from the Fourier analysis of (D) versus magnetic field. Linear fit yields an estimated *g*-factor of 0.062. Inset shows the shuttling trajectory of the spin qubit from D4 to D6. (**F**) Extended time evolution in D6 at B = 41.4 mT, yielding a qubit frequency of 34.51 MHz and a dephasing time of T_2* = 1.12 μs. The experimental trace was fitted (dashed lines) as described in (*31*), section 17. (**G** and **H**) Table and visualization of the extracted parameters *g*-factors and T_2*, respectively.

strength is non-negligible compared with the Zeeman energy difference ΔE_Z and the qubit frequency f_A, pulse shaping is essential to mitigate coherent errors (*12*, *37*). We implemented exchange pulses with a Hamming window and performed the CZ gate calibration (Fig. 2D) [(*31*), section 12].

We now advance to benchmarking a two-qubit gate in germanium by executing two-qubit randomized benchmarking [see (*31*), section 6, for further details, and section 7 for two-qubit GST]. Individual Clifford gates were implemented by sequentially applying one or more of the gates $CZ, X^{\mathrm{A(B)}}_{\pi/2}, Z^{\mathrm{A(B)}}_{\pi/2}$, and I. From the fit of the decay constants of the reference and interleaved sequence in Fig. 2E, we determined the average Clifford gate fidelity as $F_{\mathrm{Clifford2}}$ = 98.60(6)% and the average CZ gate fidelity as F_{CZ} = 99.33(10)%, consistent with the results of error modeling [(*31*), section 13]. For the single-qubit gate performance in the two-qubit space, we estimate the lower bound of fidelity, averaged between both qubits, as $\frac{1}{2}\left(F_{X_{\pi/2},\mathrm{A}} + F_{X_{\pi/2},\mathrm{B}}\right) \geq$ 99.90(5)%. We believe that these high fidelities result from the high driving efficiency and relatively long T_2* at low magnetic field.

Hopping spins to benchmark large and high-connectivity quantum dot architectures

The presented sparse occupation of a quantum dot array allows the construction of high-fidelity hopping-based quantum logic, but it may also facilitate the implementation of quantum circuits with high connectivity. Although two-dimensional quantum circuits with nearest-neighbor connectivity can already tolerate high error rates (*25*, *38*, *39*), an increased connectivity may substantially lower the physical qubit overhead and lower the logical qubit error rate (*40*). We therefore envision a qubit architecture with sparse occupation (Fig. 3A) to be a potential platform. Here, qubits may be shuttled to remote sites for distant two-qubit logic, and single-qubit logic can be executed during this trajectory.

As a first step toward such architectures, we developed and characterized an extended system comprising 10 quantum dots. The system (Fig. 3B) consists of a multilayer gate architecture with quantum dots, D*n* with *n* ∈

[[1,10]], and peripheral charge sensors, which may be integrated within the array through development of vertical interconnects such as in (*41*). By exploiting dedicated (virtual) barrier and plunger gate voltages, we prepared the quantum dots D1 and D4 in the single-hole regime, leaving the others empty [(*31*), sections 14 and 15].

The hopping-based qubit gates were used to rapidly characterize the different quantum dot *g*-factors and coherence times. After initializing the associated qubit pair Q1,Q4 into its ↑↓ eigenstate, we diabatically shuttled the Q4 spin to another quantum dot site, D*n*. We let it precess for a time $t_{\mathrm{D}n}$, after which the spin was shuttled back and read out. The misalignment between the spin quantization axes gives rise to spin rotations with the Larmor frequency $f_{\mathrm{D}n}$ (*21*). The resulting oscillations are shown as a function of waiting time in D6, t_{D6}, and magnetic field (Fig. 3D). From the linear scaling of the D6 Larmor frequency with the magnetic field, we extracted an effective *g*-factor of 0.062 (Fig. 3E) and from the decay of the oscillations a dephasing time of $T_2^* = 1.12\ \mu\mathrm{s}$ (Fig. 3F). Repeating this protocol to reach all the quantum dots, we extracted the Larmor frequency and dephasing time at each site, as displayed in Fig. 3, G and H. For the case of Q1 (Q4), we shuttled the spin to D5 (D8) back and forth twice, interleaved by a varying precession time in D1, t_{Q1} (in D4, t_{Q4}), which we explain in detail in (*31*), section 16. Our experiments showed an average T_2^* of $1.3 \pm 0.4\ \mu\mathrm{s}$ at a magnetic field of 41.4 mT [(*31*), section 17], and we attribute the fast dephasing of D9 ($T_2^* = 290$ ns) to charge noise originating from a fluctuator nearby. Furthermore, we obtained an average *g*-factor of 0.04 ± 0.03. The observed variability in this distribution is likely a result of multiple factors: the heterogeneity inherent in the shapes of the quantum dots (dot-to-dot variability), the presence of strain gradients in the quantum well arising from the gates above or the SiGe strained relaxed buffer below, and the impact of interface charges. The average *g*-factor that we obtained was considerably lower than what has been observed in the literature (*10*, *24*, *26*, *30*). We suggest that this reduction is primarily due to two phenomena: a precise in-plane magnetic field configuration and an appreciable renormalization of the gyromagnetic ratio from the pure heavy-hole value of ~0.18 (*27*, *28*, *42*). Such renormalization is driven by substantial interband mixing between the heavy-hole and the light-hole band, which we attribute to asymmetries in the strain, as simulated in (*31*), section 18. Furthermore, these simulations indicate that such a low average effective *g*-factor only occurs when the misalignment of the magnetic field is smaller than 0.1° with respect to the plane of the *g*-tensors, emphasizing the importance of accurately controlling the magnetic field orientation when operating with germanium qubits.

Conclusions

We have shown here that hopping spin qubits between quantum dots with site-dependent *g*-tensors allows for coherent shuttling with fidelities up to 99.992% per hop, single-qubit gate fidelities up to 99.97%, and two-qubit gate fidelities up to 99.3%. This method allows for efficient control with baseband pulses only and fast execution of quantum gates even at low magnetic fields where the coherence is high. Using this approach for the control of dense quantum dot arrays with sparse qubit occupation can alleviate challenges in crosstalk and heating while providing high connectivity. Recent theoretical developments predict that increased connectivity can substantially improve logical qubit performance and reduce the required overhead on physical qubits (*40*). Sparse spin qubit arrays could be particularly suited for error correction schemes requiring either a larger number of nearest neighbors or coupling beyond nearest neighbors. A substantial challenge remains in addressing the qubit-to-qubit variation. This was already highlighted in the original work by Loss and DiVincenzo (*1*). We envision that the characterization of larger qubit arrays and statistical analysis will become pivotal, with the presented 10–quantum dot array already providing a first indication that design considerations can determine relevant qubit parameters. Site-dependent quantization axes can be realized by *g*-tensor engineering such as in elongated quantum dots (*43*), by using nanomagnets, or by applying currents through nanowires above the qubit plane (*44*). The developed control methods for high timing accuracy can also advance exchange-only qubits that are operated using baseband pulses (*19*) and affect platforms such as superconducting qubits (*45*). We envision establishing high-fidelity quantum operation through low-power control in uniform and large-scale systems to be a critical step in realizing fault-tolerant quantum computing.

REFERENCES AND NOTES

1. D. Loss, D. P. DiVincenzo, *Phys. Rev. A* **57**, 120–126 (1998).
2. G. Burkard, T. D. Ladd, A. Pan, J. M. Nichol, J. R. Petta, *Rev. Mod. Phys.* **95**, 025003 (2023).
3. F. H. L. Koppens *et al*., *Nature* **442**, 766–771 (2006).
4. M. Veldhorst *et al*., *Nat. Nanotechnol.* **9**, 981–985 (2014).
5. M. Pioro-Ladrière, Y. Tokura, T. Obata, T. Kubo, S. Tarucha, *Appl. Phys. Lett.* **90**, 024105 (2007).
6. J. Yoneda *et al*., *Nat. Nanotechnol.* **13**, 102–106 (2018).
7. D. V. Bulaev, D. Loss, *Phys. Rev. Lett.* **98**, 097202 (2007).
8. S. Nadj-Perge, S. M. Frolov, E. P. A. M. Bakkers, L. P. Kouwenhoven, *Nature* **468**, 1084–1087 (2010).
9. K. Wang *et al*., *Nat. Commun.* **13**, 206 (2022).
10. N. W. Hendrickx, D. P. Franke, A. Sammak, G. Scappucci, M. Veldhorst, *Nature* **577**, 487–491 (2020).
11. A. Noiri *et al*., *Nature* **601**, 338–342 (2022).
12. X. Xue *et al*., *Nature* **601**, 343–347 (2022).
13. S. G. J. Philips *et al*., *Nature* **609**, 919–924 (2022).
14. K. Takeda *et al*., *NPJ Quantum Inf.* **4**, 54 (2018).
15. B. Undseth *et al*., *Phys. Rev. Appl.* **19**, 044078 (2023).
16. B. Undseth *et al*., *Phys. Rev. X* **13**, 041015 (2023).
17. M. Russ, G. Burkard, *J. Phys. Condens. Matter* **29**, 393001 (2017).
18. R. W. Andrews *et al*., *Nat. Nanotechnol.* **14**, 747–750 (2019).
19. A. J. Weinstein *et al*., *Nature* **615**, 817–822 (2023).
20. G. Scappucci *et al*., *Nat. Rev. Mater.* **6**, 926–943 (2021).
21. F. van Riggelen-Doelman *et al*., *Nat. Commun.* **15**, 5716 (2024).
22. B. Jadot *et al*., *Nat. Nanotechnol.* **16**, 570 (2021).
23. W. I. L. Lawrie *et al*., *Nat. Commun.* **14**, 3617 (2023).
24. N. W. Hendrickx *et al*., *Nat. Mater.* 10.1038/s41563-024-01857-5 (2024).
25. A. G. Fowler, M. Mariantoni, J. M. Martinis, A. N. Cleland, *Phys. Rev. A* **86**, 032324 (2012).
26. D. Jirovec *et al*., *Phys. Rev. Lett.* **128**, 126803 (2022).
27. C.-A. Wang, G. Scappucci, M. Veldhorst, M. Russ, Modelling of planar germanium hole qubits in electric and magnetic fields. arXiv: 2208.04795 [cond-mat.mes-hall] (2022).
28. J. C. Abadillo-Uriel, E. A. Rodríguez-Mena, B. Martinez, Y.-M. Niquet, *Phys. Rev. Lett.* **131**, 097002 (2023).
29. C. Corley-Wiciak *et al*., *ACS Appl. Mater. Interfaces* **15**, 3119–3130 (2023).
30. N. W. Hendrickx *et al*., *Nature* **591**, 580–585 (2021).
31. Materials and methods are available as supplementary materials online.
32. M. Reed, Dissertation, Yale University, New Haven, CT (2013).
33. L. M. K. Vandersypen *et al*., *NPJ Quantum Inf.* **3**, 34 (2017).
34. E. Nielsen *et al*., *Quantum Sci. Technol.* **5**, 044002 (2020).
35. R. Blume-Kohout *et al*., *Nat. Commun.* **8**, 14485 (2017).
36. J. P. Dehollain *et al*., *New J. Phys.* **18**, 103018 (2016).
37. M. Rimbach-Russ, S. G. J. Philips, X. Xue, L. M. K. Vandersypen, *Quantum Sci. Technol.* **8**, 045025 (2023).
38. D. S. Wang, A. G. Fowler, L. C. L. Hollenberg, *Phys. Rev. A* **83**, 020302 (2011).
39. B. Hetényi, J. R. Wootton, Creating entangled logical qubits in the heavy-hex lattice with topological codes. arXiv:2404.15989 [quant-ph] (2023).
40. S. Bravyi *et al*., *Nature* **627**, 778–782 (2024).
41. W. Ha *et al*., *Nano Lett.* **22**, 1443–1448 (2022).
42. B. Martinez, J. C. Abadillo-Uriel, E. A. Rodriguez-Mena, Y.-M. Niquet, *Phys. Rev. B* **106**, 235426 (2022).
43. S. Bosco, M. Benito, C. Adelsberger, D. Loss, *Phys. Rev. B* **104**, 115425 (2021).
44. R. Li *et al*., *Sci. Adv.* **4**, eaar3960 (2018).
45. D. L. Campbell *et al*., *Phys. Rev. X* **10**, 041051 (2020).
46. C.-A. Wang *et al*., Data and code for: Operating semiconductor quantum processors with hopping spins, 4TU.ResearchData repository (2024); https://doi.org/10.4121/158ba07a-4375-4c17-bf7b-289726f5452a.v2.

ACKNOWLEDGMENTS

We are grateful to B. Undseth, I. F. de Fuentes, X. Xue, E. Raymenants, C. Ostrove, Y.-M. Niquet, and J. C. Abadillo-Uriel for fruitful discussions and L. M. K. Vandersypen for proofreading. **Funding:** This work was supported by the Dutch Research Council (NWO) through an ENW grant, the European Union through ERC Starting Grant QUIST 850641, and through the IGNITE project of European Union's Horizon Europe Framework Programme under grant 101069515. F.B. acknowledges support from the NWO through the National Growth Fund program Quantum Delta NL (grant NGF.1582.22.001). N.W.H. acknowledges support from the European Union through EIC Transition Grant GROOVE 101113173. M.R.-R. acknowledges support from the NWO under Veni grant VI.Veni.212.223. This research was sponsored in part by the Army Research Office (ARO) under awards W911NF-23-1-0110 and W911NF-17-1-0274. The views, conclusions, and recommendations contained in this document are those of the authors and are not necessarily endorsed nor should they be interpreted as representing the official policies, either expressed or implied, of the Army Research Office (ARO) or the US Government. The US Government is authorized to reproduce and distribute reprints for Government purposes notwithstanding any copyright notation herein. **Author contributions:** C.-A.W., V.J., H.T., C.X.Y., A.I., and F.B. conducted the experiments. C.-A.W. and F.B. analyzed the data. C.-A.W., C.D., B.D.W., M.F., and M.R.-R. performed the simulations and theoretical analysis. W.I.L.L. and S.D.O. fabricated the devices. V.J., C.X.Y., F.B., F.v.R.-D., and N.W.H. contributed to device development and measurement setups. S.L.d.S developed the measurement software. L.E.A.S., A.S., and G.S. supplied the heterostructures. C.-A.W., F.B., and M.V. wrote the manuscript with input from all authors. M.V. and F.B. supervised the project. **Competing interests:** N.W.H. is also affiliated with

Groove Quantum BV and declares equity interest. N.W.H. and M.V. are inventors on a patent application (NL provisional application N2036660) submitted by Delft University of Technology related to controlling semiconductor qubits. The remaining authors declare no competing interests. **Data and materials availability:** All data are available in the main manuscript or supplementary materials or have been deposited at the 4TU.ResearchData repository (*46*).

SUPPLEMENTARY MATERIALS

science.org/doi/10.1126/science.ado5915
Materials and Methods
Supplementary Text
Figs. S1 to S26
Tables S1 to S9
References (*47*–*70*)

Submitted 12 February 2024; accepted 14 June 2024
10.1126/science.ado5915